

In Situ Defect Induction in Close-Packed Lattice Plane for the Efficient Zinc Ion Storage

Xuefang Xie, Guozhao Fang,* Wenjie Xu, Jialin Li, Mengqiu Long, Shuquan Liang, Guozhong Cao, and Anqiang Pan*

In situ electrochemical activation brings unexpected electrochemical performance improvements to electrode materials, but the mechanism behind it still needs further study. Herein, an electrochemically in situ defect induction in close-packed lattice plane of vanadium nitride oxide (VN_xO_y) in aqueous zinc-ion battery is reported. It is verified by theoretical calculation and experiment that the original compact structure is not suitable for the insert of Zn^{2+} ion, while a highly active one after the initial electrochemical activation accompanied by the in situ defect induction in close-packed lattice plane of VN_xO_y exhibits efficient zinc ion storage. As expected, activated VN_xO_y can achieve very high reversible capacity of $231.4 \text{ mA h g}^{-1}$ at 1 A g^{-1} and cycle stability upto 6000 cycles at 10 A g^{-1} with a capacity retention of 94.3%. This work proposes a new insight for understanding the electrochemically in situ transformation to obtain highly active cathode materials for the aqueous zinc-ion batteries.

1. Introduction

Aqueous zinc-ion batteries (ZIBs) have been widely concerned because of their low cost, environmental protection, and high safety.^[1] Nevertheless, compared with the common monovalent ions (Li^+ or Na^+), the strong electrostatic interaction

X. Xie, Dr. G. Fang, Prof. S. Liang, Prof. A. Pan
School of Materials Science and Engineering
Central South University
Changsha, Hunan 410083, P. R. China
E-mail: fg_zhao@csu.edu.cn; pananqiang@csu.edu.cn

Dr. G. Fang, Prof. S. Liang, Prof. A. Pan
Key Laboratory of Electronic Packaging and Advanced Functional
Materials of Hunan Province
Central South University
Changsha, Hunan 410083, P. R. China

W. Xu
Frontier Institute of Science and Technology
Xi'an Jiaotong University
Xi'an, Shanxi 710054, P. R. China

J. Li, Prof. M. Long
School of Physics and Electronics
Central South University
Changsha, Hunan 410083, P. R. China

Prof. G. Cao
Department of Materials Science & Engineering
University of Washington
Seattle, WA 98195, USA

 The ORCID identification number(s) for the author(s) of this article can be found under <https://doi.org/10.1002/sml.202101944>.

DOI: 10.1002/sml.202101944

between Zn^{2+} and cathode materials will lead to a higher energy barrier for Zn^{2+} migration, especially in dense crystal structure. It often causes the sluggish kinetics, the phase transition, and even the deterioration of the structure, then resulting in unsatisfactory electrochemical performance.^[2] Similar features also plague other multivalent-ion batteries, such as magnesium-ion batteries and aluminum-ion batteries.^[3] It was reported that designing defects into cathode can improve the Zn^{2+} diffusion kinetics,^[3c,4] however, it is still a great challenge to fabricate the proper cathode materials with defects artificially.

The electrochemical performance of many cathode materials in ZIBs was

greatly improved after electrochemical activation during cycling process, which was often accompanied by the in situ phase transformation. In electrochemical activation process, the cathode material often transforms from a compact structure to a loose structure, such as V_2O_5 to $\text{V}_2\text{O}_5 \cdot n\text{H}_2\text{O}$,^[5] Mn_3O_4 to $\text{A}_x\text{MnO}_2 \cdot n\text{H}_2\text{O}$,^[6] $\beta\text{-MnO}_2$ to $\text{B-Zn}_x\text{MnO}_2 \cdot n\text{H}_2\text{O}$,^[7] $\alpha\text{-MnO}_2$ to ZnMn_2O_4 ,^[8] etc. Generally, this kind of materials have better structural stability and cycle stability compared to that of original one.^[6,9] Unfortunately, the in-depth study to reveal the mechanism behind this electrochemical activity is rarely reported.

Herein, we reported an electrochemically in situ defect induction in close-packed lattice plane of vanadium nitride oxide (VN_xO_y) for efficient zinc ion storage. Density functional theory (DFT) calculations clarified that the original compact structure is not suitable for the insert of Zn ion, while the existence defects in the close-packed lattice plane can provide available insertion channels and active sites for Zn ion diffusion. After electrochemically in situ activation, it converted from the electrochemically inert VN_xO_y into a highly electrochemically active one for aqueous ZIBs. The activated VN_xO_y exhibited a high capacity of $231.4 \text{ mA h g}^{-1}$ at 1.0 A g^{-1} , a good rate capability of 221 mA h g^{-1} at 5.0 A g^{-1} , and an ultrastability up to 6000 cycles at 10 A g^{-1} .

2. Results and Discussion

2.1. Material Preparation and Characterization

A spindle-shaped VN_xO_y with a core-shell structure as ZIB cathode was reported for the first time in this article. In a typical

synthesis, the precursor MIL-88B (V) was first prepared according to the previous report,^[10] and its X-ray diffraction (XRD) pattern is shown in Figure S1, Supporting Information. Then the MIL-88B (V) mixed with or without melamine (as a nitrogen source) was calcined in argon to obtain the final products (Figure 1a). The effects of different content of nitrogen sources and calcination temperatures on their structures and morphologies were revealed. The XRD pattern of final product obtained at 800 °C without nitrogen source is shown in Figure 1b, which exhibits a rhombohedral V₂O₃ phase [Space group R-3c (167), JCPDS No. 34-0187]. By adjusting the mass ratio of precursor to melamine to 1:0.5, VN/V₂O₃ composite that is composed of the face centered cubic (fcc) VN phase [space group Fm-3m (225), JCPDS No. 73-2038] and V₂O₃ phase (Figure 1c) was appeared. With the further increase of melamine (1:4 mass ratio), we obtained a VN_xO_y compound, in which all the characteristic peaks in XRD pattern (Figure 1d) have a good correspondence with the fcc VN phase. The XRD patterns of VN_xO_y at different calcination temperatures are shown in Figure S2, Supporting Information. Weak diffraction peaks can be seen at 600 °C, and as the temperature increases, the crystallinity of the samples is improved.

The scanning electron microscopy (SEM) and transmission electron microscopy (TEM) were conducted to characterize the morphology of the synthesized products. As shown in Figure S3, Supporting Information, the SEM and TEM of MIL-88B(V) are spindle-shaped nanorods with a length of ≈5–15 μm. After calcination at 800 °C, the final products largely maintained the

spindle-shaped morphology of the precursor. When melamine is not added, the V₂O₃ was a solid shuttle shape with some small burr on the surface (Figure 2a). The lattice fringes of 1, 2, 3 marked in Figure 2b belong to the (202), (110), and (113) planes of V₂O₃ phase, respectively. Figure 2c shows the element mapping image of V₂O₃ sample, confirming uniform distribution of V, O, and C elements. The N₂ adsorption/desorption measurement results show that the specific surface area of V₂O₃ is 228.07 m² g⁻¹ (Figure 2d). The VN/V₂O₃ sample was also characterized by TEM image (Figure 2e), which can be seen that the structure of VN/V₂O₃ is porous. The lattice fringe of 1 marked in Figure 2f matches well with the (111) plane of VN, while the 2 and 3 represent (104) and (113) planes of V₂O₃, respectively. Figure 2g shows the element mapping image of VN/V₂O₃ sample, confirming the uniform distribution of V, N, O, and C elements. The specific surface area of VN/V₂O₃ is 254.32 m² g⁻¹ and the aperture is ≈4 nm (Figure 2h). When the mass ratio of precursor to melamine is 1:4, the morphology of the sample has undergone great changes, becoming a spindle-shaped nanorod with core-shell structure, as shown in Figure 2i. The planes of 1, 2, and 3 marked in the figure belong to (111) and (200) crystal planes of VN phase, respectively (Figure 2j). The element mapping images also reveal the uniform distribution of V, N, O, and C elements in the core-shell spindle-shaped nanorod (Figure 2k). In addition, the specific surface area of VN_xO_y is 424.67 m² g⁻¹ (Figure 2l), which is much higher than that of V₂O₃ and VN/V₂O₃ (Table S1, Supporting Information). The

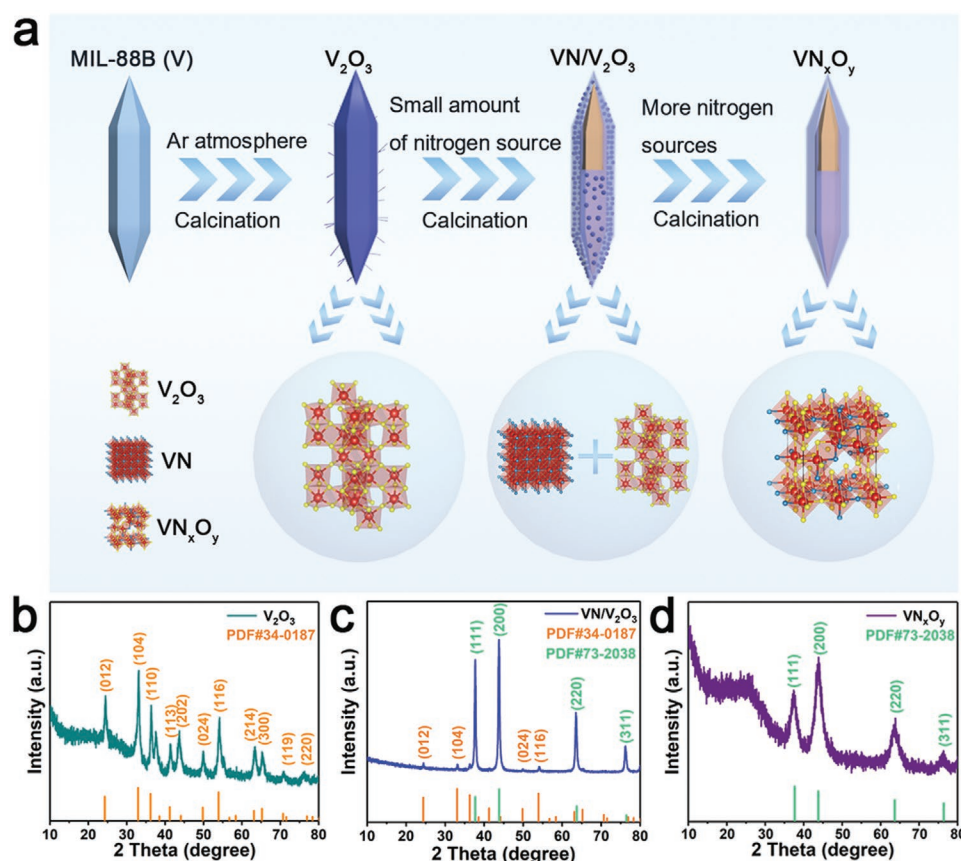


Figure 1. a) Schematic illustration of the synthetic process and the corresponding XRD patterns of b) V₂O₃, c) VN/V₂O₃, and d) VN_xO_y at 800 °C for 3 h.

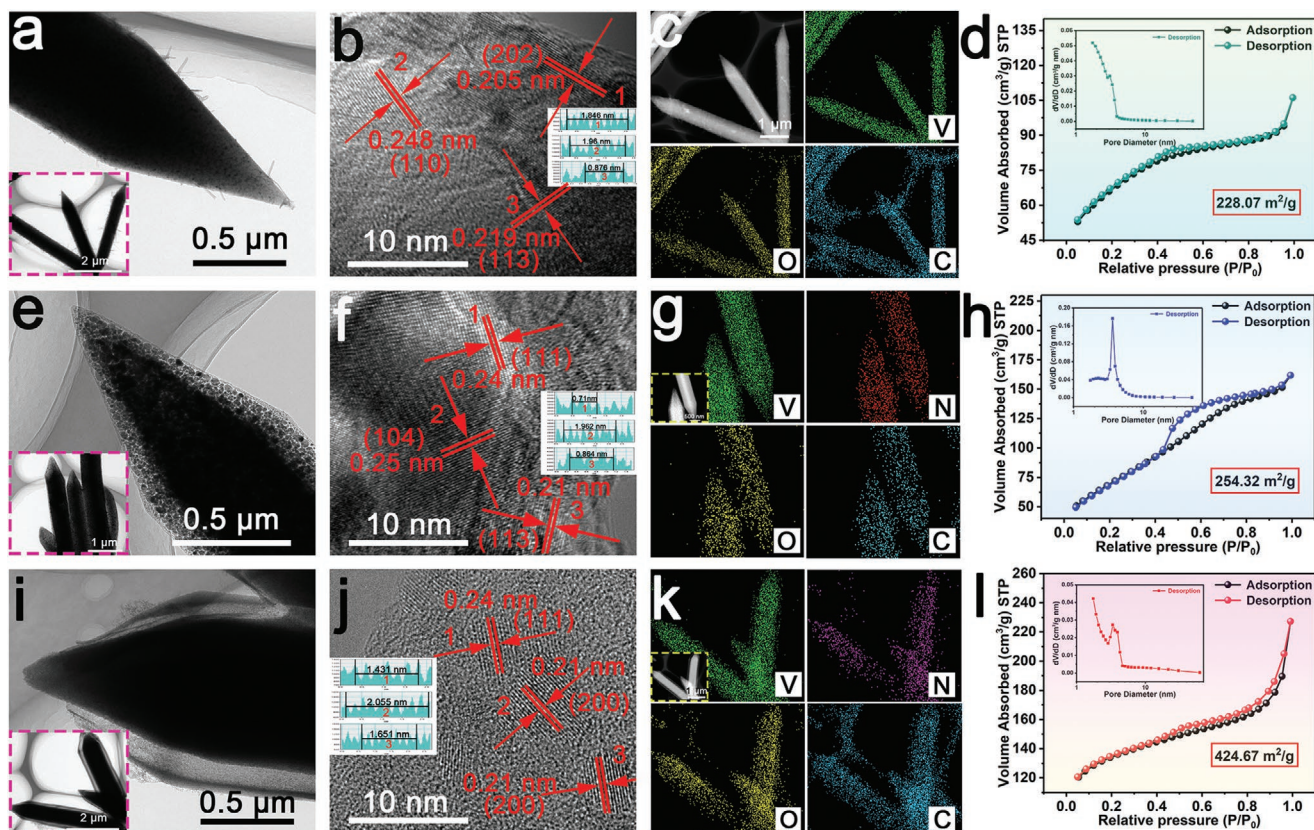


Figure 2. a,e,i) TEM image, b,f,j) HRTEM image, c,g,k) element mappings, d,h,l) the nitrogen adsorption-desorption isotherms and corresponding pore size distribution curves of a–d) V_2O_5 , e–h) VN/V_2O_5 , i–l) VN_xO_y , respectively.

VN_xO_y electrode with a core-shell spindle-shaped structure can provide more contact area between the electrode surface and the electrolyte, which is conducive to enhancing mass transfer. In addition, this core-shell structure provides a large space, which is beneficial for the transformation of the crystal phase without destroying the original structure. At the same time, it also laid the foundation for stable electrochemical performance.

2.2. In Situ Phase Transition Analysis

It can be seen from **Figure 3a** that the specific capacity of VN_xO_y at initial discharge is less than 100 mA h g^{-1} . However, a very long quasi-plateau at $\approx 1.5 \text{ V}$ was observed during the charging process. It may be due to an electrochemical activation during initial charging process.^[9b] In order to explore the structural evolution of VN_xO_y , ex situ XRD patterns of VN_xO_y electrodes during initial cycle were conducted (**Figure 3b**). It can be clearly seen that the peaks of the (111) plane gradually shift left during the first discharging, when charging to 1.6 V, the peak gradually shifts to the right, accompanied by a weakening of peak intensity. However, there is no obvious change of the (200) plane. The XRD spectra of VN/V_2O_5 at initial state, discharge to 0.2 V, and charging to 1.6 V are shown in **Figure S4**, Supporting Information. After charging to 1.6 V for the first time, the VN/V_2O_5 electrode also undergoes an electrochemical activation process. X-ray photoelectron spectroscopy

(XPS) was performed to identify the valence state of VN_xO_y at different states (**Figure S5**, Supporting Information). In the high-resolution Zn 2p spectra (**Figure 3c**), two strong peaks with binding energies of 1021.8 and 1044.8 eV appeared in the fully discharged state (0.2 V), but became very weak in the fully charged state (1.6 V), indicating that Zn^{2+} is basically inserted/removed from the VN_xO_y host. It was reported that the nitrogen with low electronegativity tends to form weak bonds with Zn^{2+} ion.^[11] **Figure 3d** shows the XPS V 2p spectrum in the initial state, where the peaks at 517.5 and 524.8 eV correspond to V 2p_{3/2} and V 2p_{1/2} of V^{5+} , respectively.^[12] The peaks at 516.7 and 522.9 eV are V 2p_{3/2} and V 2p_{1/2} of V^{4+} .^[13] The peak at 514.2 at V 2p_{3/2} is a mixed valence state of V^{3+}/V^{4+} .^[14] This peak is formed after charging to 1.6 V, indicating that a change in the valence state of V has occurred during the electrochemical activation. This coincides with the small amount of V^{3+} precipitation in **Figure 3h**. The high resolution of the N 1s spectra are mainly represented by three nitrogens, which correspond to the graphitized N (400.4 eV), pyridinic/pyrrolic N (398.9 eV), and $N^{3-}-V$ (397.2 eV) (**Figure 3e**). When the battery is fully discharged, the peak of $N^{3-}-V$ shifted to a higher binding energy (398.0 eV), which corresponds to the binding energy of the $N^{2-}-V$ bond.^[15] When the battery is charged to 1.6 V, the peak of $N^{3-}-V$ returned to its original state. The peaks of graphitic N and pyridinic/pyrrolic N have not changed, and they may originate from the carbon layer.^[16] In VN_xO_y , the bond between Zn^{2+} and N atoms does not produce strong ionic bond, so Zn^{2+}

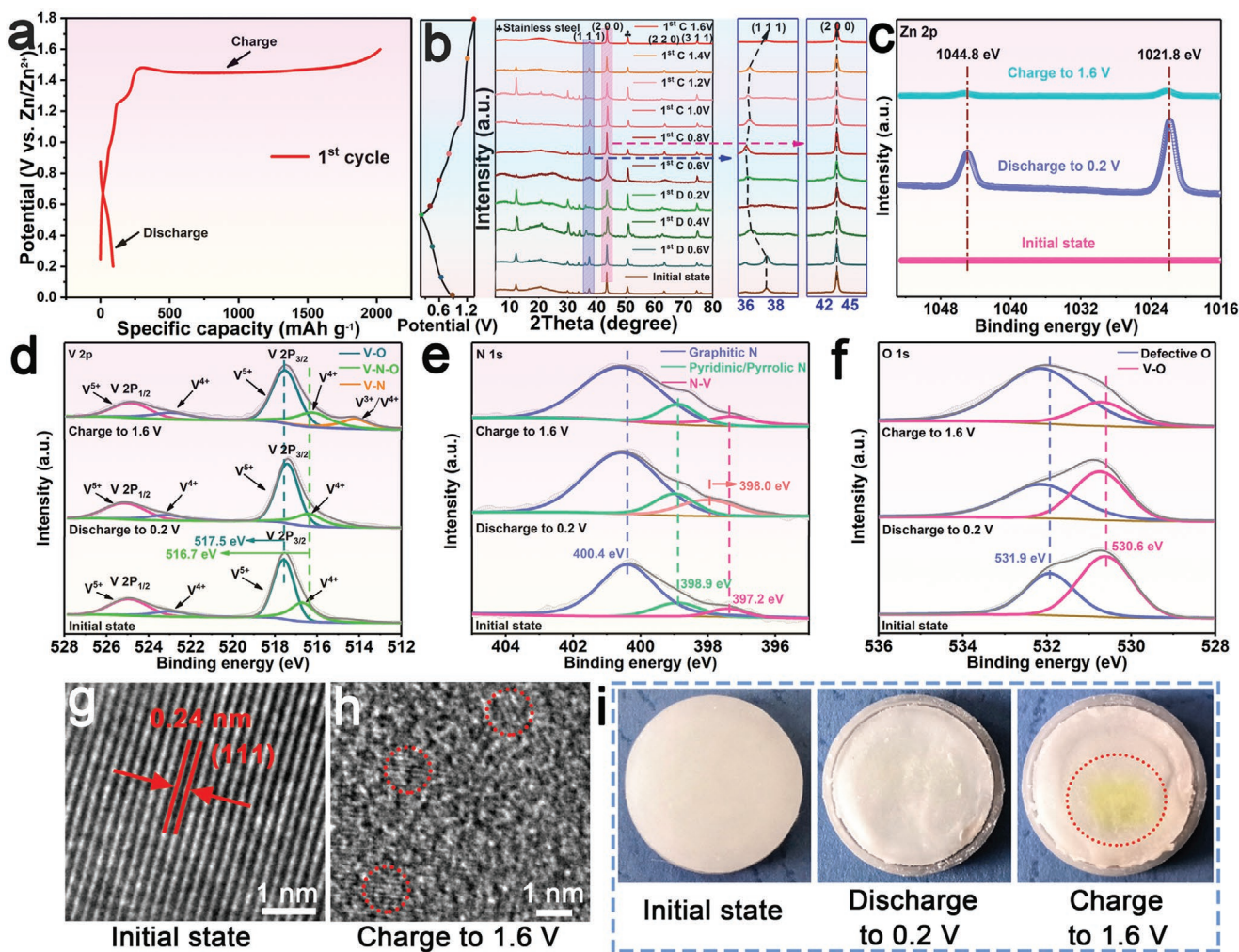


Figure 3. a) The initial discharge/charge profiles at 0.1 A g^{-1} of VN_xO_y . b) Ex situ XRD patterns of VN_xO_y electrodes during initial cycle. Ex situ XPS spectra of VN_xO_y at different charging/discharging states for c) high-resolution Zn 2p spectra, d) high-resolution V 2p spectra, e) high-resolution N 1s spectra, f) high-resolution O 1s spectra. HRTEM image of VN_xO_y electrode g) in initial state and h) after initially charging to 1.6 V. i) Optical photograph of membrane in different charging and discharging states.

is easy to release without structural damage. In addition, the valence state of N shows reversible electrochemical behavior after the release of Zn^{2+} . We also found that after the initial charging progress, the proportion of defective oxygen increased significantly (Figure 3f).

According to the above discussion, it can be inferred that the electrochemical activation of VN_xO_y during the initial cycling is related to the deformation of close-packed (111) plane. During the discharge process, zinc ions easily enter the interlayer between (111) planes of fcc phase compared to other planes, which may cause the distortion of (111) planes. As a result, after the zinc ion is released during charge process, vanadium atoms are also readily released from the structure, with an increase in defective oxygen. This situation is similar to previous reports on MnO, in which Mn atoms dissolved in the initial charging.^[9b] In order to further confirm that the material has defects after charging to 1.6 V, HRTEM image analysis was carried out. In the initial state, the ordered lattice fringes are clearly visible, and the (111) interplanar spacing of the VN phase is 0.24 nm

(Figure 3g). HRTEM image of VN_xO_y electrode charged to 1.6 V confirmed that the structure exhibits a disorder of a large number of defects compared to the original one (Figure 3h). When charging to 1.6 V, the membrane appears the yellow substance, indicating that a small amount of V^{3+} dissolves out, as shown in Figure 3i. After the initial electrochemical activation, VN_xO_y electrode exhibits the reversible electrochemical behavior, which will be discussed later.

First-principles calculation was conducted in order to further understand the mechanism of this electrochemical activation. The design of our calculation structure is reasonable and consistent with the experimental results of XPS, in which the atomic ratio of V, N, O in the VN_xO_y after activation is $\approx 1.0:1.1:2.1$. Interestingly, when Zn^{2+} ions are inserted into the perfect crystal structure of VN, the structure is destroyed (Figure 4a). It is also found that this process is an endothermic reaction, indicating that Zn^{2+} ions are not easily embedded into fcc VN. That is why the first discharge capacity of VN_xO_y with complete fcc phase is so low. When Zn^{2+} ions are inserted into

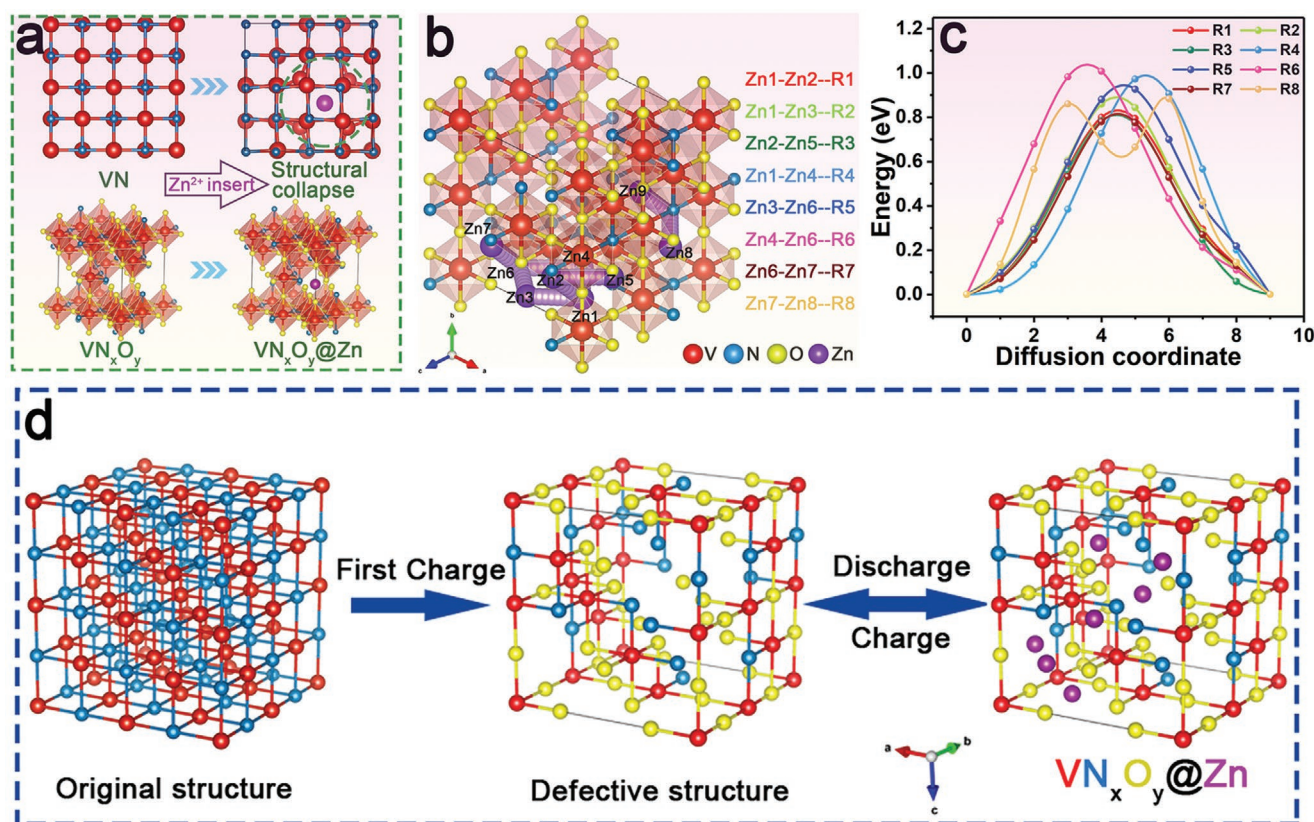


Figure 4. a) Crystal structure of defect-free vanadium nitride and VN_xO_y with defect after Zn ion intercalation (The green circle shows structural collapse). b) The diffusion pathways of Zn ion in the defect vanadium nitride and c) the corresponding diffusion activation barriers of Zn ion. d) Schematic diagram of zinc storage mechanism of vanadium oxynitride.

the crystal structure of VN_xO_y with defects in (111) planes, the reaction is exothermic, indicating that defective VN_xO_y is more suitable for the insertion and extraction of Zn ions (Figure S6 and Table S2, Supporting Information). This further indicates that the vacancy and defect produced by VN_xO_y in charging state is easier to diffuse Zn^{2+} . The activation barrier of V_2O_3 was calculated and the results are shown in Figure S7, Supporting Information. The activation barrier is ≈ 1.46 eV. The specific calculation formula and energy value are in the experimental part and Table S3, Supporting Information. The nudged elastic band (NEB) method was further used to study the internal diffusion of Zn^{2+} ions at different positions in the defective VN_xO_y structure (Figure 4b). The diffusion energy barriers corresponding to different paths are shown in Figure 4c, which indicates that it is possible for Zn^{2+} ions to migrate into VN_xO_y crystal structure with vacancy and defect, and the activation barrier is ≈ 0.8 eV. We simulated eight diffusion paths, Zn1-Zn2, Zn1-Zn3, Zn2-Zn5, Zn1-Zn4, Zn3-Zn6, Zn4-Zn6, Zn6-Zn7, Zn7-Zn8 correspond to R1-R8 paths respectively. It can be seen that the diffusion activation barriers are lower where there are defects on the close-packed (111) plane, which indicates that the defects on the close-packed (111) plane are conducive to the diffusion of Zn ions. This further explains that in situ electrochemical activation is a feasible method for high-efficiency energy storage of zinc ion batteries. Figure 4d shows the schematic diagram of a zinc ion battery with VN_xO_y as cathode, zinc foil as anode, and

3 M of zinc sulfate aqueous solution as electrolyte. The cathode part is the schematic diagram of the conversion process of VN_xO_y in the initial charging process.

As shown in Figure 5a, the electrochemical activation plateau disappeared during the subsequent charging process. In the second cycle, a quasi-plateau of ≈ 0.85 V and ≈ 1.0 V was formed with a high discharged specific capacity of 351 mA h g^{-1} . It indicates that the electrode was activated during the initial charging process. From Figures 5b,c, it can be seen that similar phenomena also occur in $\text{VN}/\text{V}_2\text{O}_3$ and V_2O_3 electrode materials, which also confirm that the electrochemical activation is beneficial to the storage of zinc. Figure 5d shows the first four cyclic voltammetry (CV) curves of VN_xO_y with a scan rate of 0.1 mV s^{-1} , showing multiple redox peaks, is consistent with the discharge/charge curve (Figure 5a). For VN_xO_y electrodes, there are two main reduction peaks at 0.615 and 1.066 V during the cathode process, and three main oxidation peaks at 0.792 V, 1.041, and 1.244 V during the anode process. The CV curve of the VN_xO_y electrode does not change significantly after the second cycle, indicating a highly reversible insertion/extraction process of Zn^{2+} . In Figure 5f, the CV curve behavior of the V_2O_3 electrode is similar to that of the VN_xO_y electrode, which is beneficial to improve the reaction kinetics after electrochemical activation. In contrast, the $\text{VN}/\text{V}_2\text{O}_3$ electrode presents redox peaks with a large polarization behavior, which has an irreversible effect in the subsequent cycle (Figure 5e).

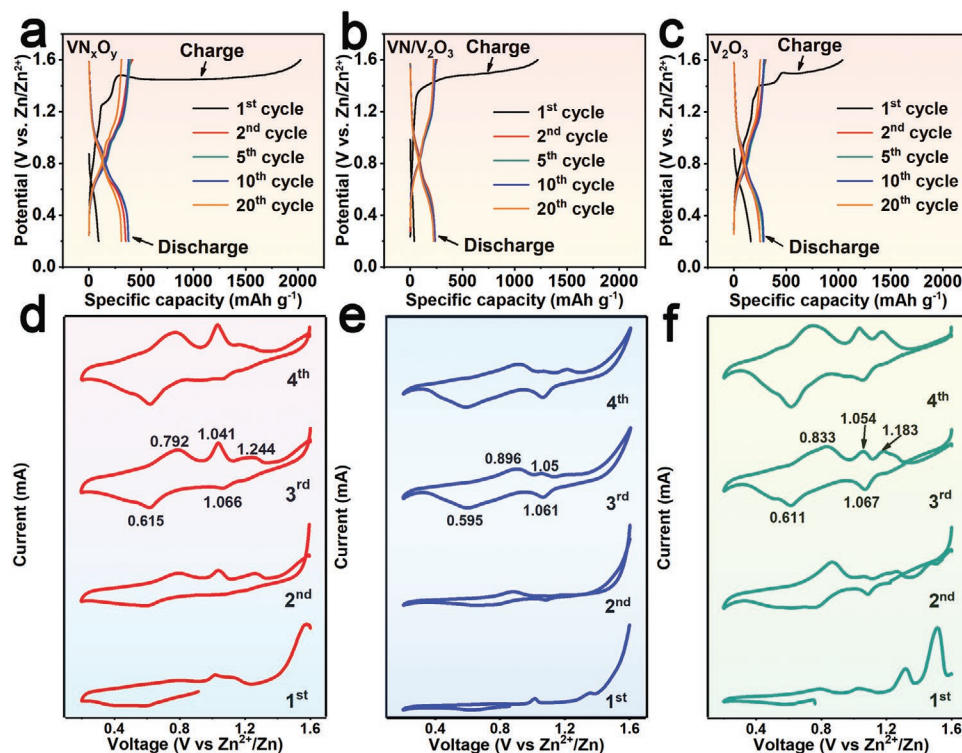


Figure 5. a–c) The selected discharge/charge profiles at 0.1 A g^{-1} and d–f) CV curves of a, d) VN_xO_y , b, e) $\text{VN}/\text{V}_2\text{O}_3$ and c, f) V_2O_3 .

2.3. Electrochemical Performance

We further evaluated the electrochemical performance of the VN_xO_y , $\text{VN}/\text{V}_2\text{O}_3$, and V_2O_3 electrodes. The cyclic voltammetry measurements of VN_xO_y at different scanning rates from 0.1 to 1.0 mV s^{-1} were performed, as shown in Figure 6a. When the scan rate is increased to 1.0 mV s^{-1} , the four obvious characteristic peaks widen, and the anode peaks shift to the positive peak and the cathode peaks to the negative peak. It can be seen that the peaks shift slightly when the scan rate increases, and the curve basically maintains a similar shape. This indicates that VN_xO_y has good kinetics and low polarization at high scan rates. In addition, the study of the electrochemical carrier transfer process usually considers the relationship between the peak current (i) and the scan rate (ν).^[17]

$$i = a\nu^b \quad (1)$$

$$i(V) = k_1\nu + k_2\nu^{1/2} \quad (2)$$

Where the b value can reveal its storage mechanism, and the range of the b value can be obtained by the slope of the $\log(\nu)$ - $\log(i)$ curve. The value of b is in the range of 0.5 – 1 . When the value of b is close to 0.5 or 1 , it indicates that the zinc storage process can be regarded as a process dominated by ion diffusion or a capacitive process. The a and b are two adjustable values.

The b values of the VN_xO_y electrodes at peaks 1, 2, 3, and 4 were calculated to be 0.929 , 0.902 , 0.976 , and 0.983 , respectively (Figure 6b). where $k_1\nu$ and $k_2\nu^{1/2}$ represent capacitive and ionic diffusion contribution. Based on formula 2, the slope can

be calculated, and the capacitance contribution rate at different scan rates can be obtained by linear fitting. Figure 6c shows the percentage of pseudo-capacitance contribution at different scan rates. As the scan speed increases, the pseudo-capacitance contribution increases gradually. According to calculations, at 1.0 mV s^{-1} , the contribution of capacitance control is 97.7% , which indicates that the partial capacitance contribution of the VN_xO_y electrode can make it have a higher rate capacity. For comparison, we also calculated the percentage of capacitive contribution of $\text{VN}/\text{V}_2\text{O}_3$ and V_2O_3 electrodes at different scan rates, and are shown in Figure S8 and Figure S9, Supporting Information, respectively, which are much smaller than the percentage of VN_xO_y capacitive contribution. This result explains why VN_xO_y has better rate performance than $\text{VN}/\text{V}_2\text{O}_3$ and V_2O_3 . The capacitance contribution of VN_xO_y at 700 and $900 \text{ }^\circ\text{C}$ is shown in Figures S10 and S11, Supporting Information.

Figure 6d compares the rate performance of these three samples. When cycling at current densities of 0.05 , 0.1 , 0.2 , 0.5 , 1.0 , 2.0 , and 5.0 A g^{-1} , the VN_xO_y electrode delivers high discharge specific capacities of 336.25 , 310.31 , 291.65 , 276.36 , 265.28 , 251.16 , and $204.22 \text{ mA h g}^{-1}$, respectively. According to the cycle data of Figure S12, Supporting Information, the initial discharge capacity of VN_xO_y electrode is 85.8 mA h g^{-1} at the current density of 1 A g^{-1} . The capacity became stable after 60 cycles. After 300 cycles, the discharge capacity is $231.4 \text{ mA h g}^{-1}$, the capacity remains at 88.6% , and the cycle coulomb efficiency is close to 100% . The capacity gradually increased in the first few cycles, which may be related to the gradual activation of the electrodes.^[18] Contrastingly, $\text{VN}/\text{V}_2\text{O}_3$ electrode delivers an initial capacity of 21.9 mA h g^{-1} and a

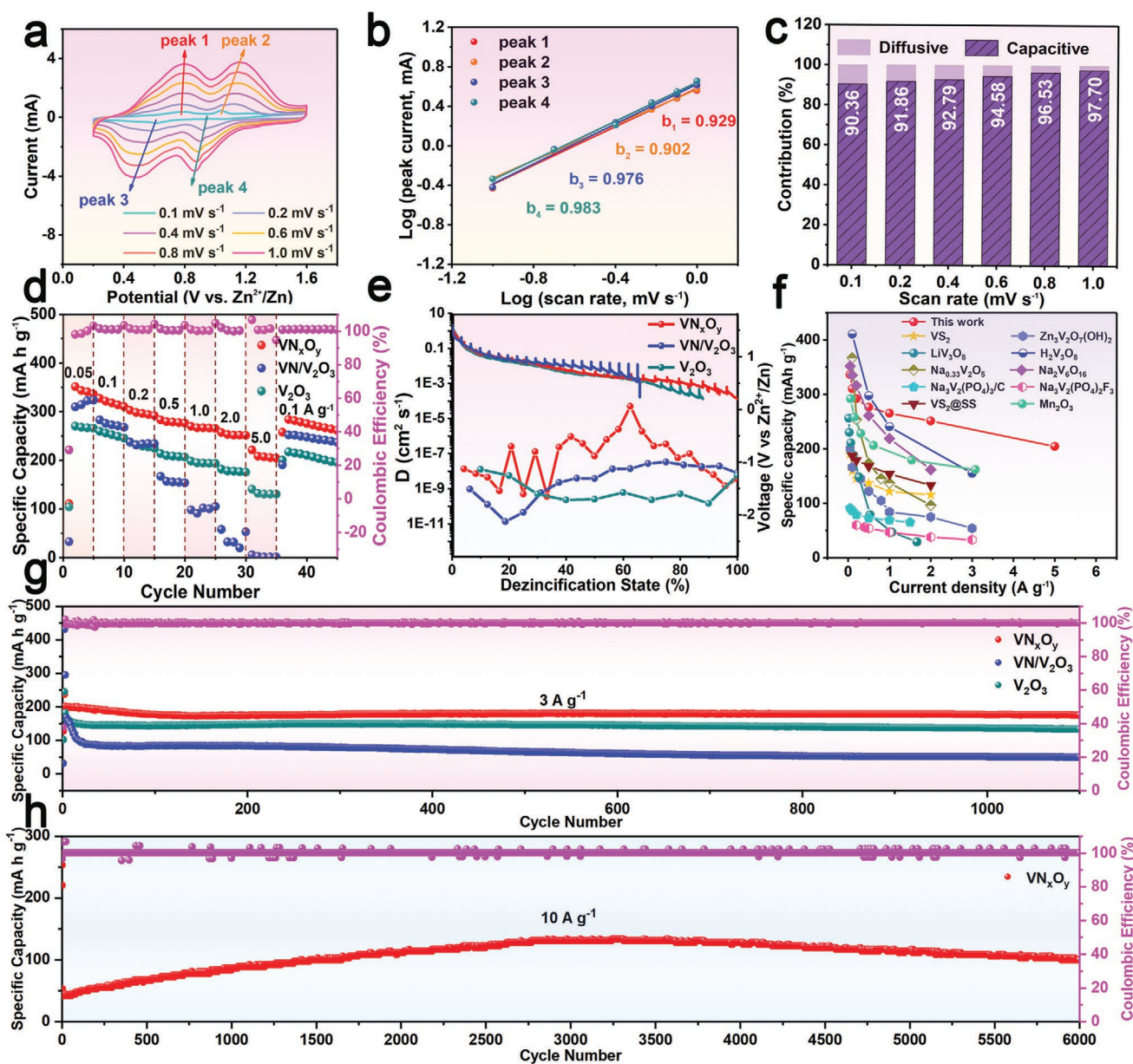


Figure 6. a) CV curves of VN_xO_y sample scanned at 0.1–1.0 mV s^{-1} , b) Corresponding log (i) versus log (v) plots at specific peak currents, c) the percent of pseudocapacitive at different scan rates. d) Rate performances and e) GITT curves and the corresponding ion diffusion coefficients during the first discharge process of the VN_xO_y , $\text{VN}/\text{V}_2\text{O}_3$, and V_2O_3 . f) Comparison plot of rate performance with previous works. Long term cycling performance at g) 3 A g^{-1} and h) 10 A g^{-1} .

capacity of 59.1 mA h g^{-1} after 300 cycles. The capacity of the V_2O_3 electrode was 147.8 mA h g^{-1} after 300 cycles.

We further evaluated the electrochemical stability of VN_xO_y , a large current density test was performed, and the results are shown in Figure 6g,h. Before the 3 A g^{-1} and 10 A g^{-1} current density cycle, the first two cycles were cycled at 0.1 A g^{-1} . Aside from the first two cycles at 0.1 A g^{-1} and the transition cycle (third cycle) from 0.1 A g^{-1} to 3 A g^{-1} , VN_xO_y has a capacity of 196.8 mA h g^{-1} in the fourth cycle. After 1100 cycles, the capacity was retained at 175 mA h g^{-1} , the retention capacity was up to 89%, and the capacity decay rate per cycle was only 0.08% (Figure 6g). The electrodes $\text{VN}/\text{V}_2\text{O}_3$ and V_2O_3 have capacities

of 49.2 and 133.4 mA h g^{-1} after 1100 cycles, respectively. In addition, when the current density is 10 A g^{-1} (Figure 6h), the specific capacity of VN_xO_y becomes stable when it is cycled for 2500 cycles, with a specific capacity of 122.2 mA h g^{-1} , and a specific capacity of 100.2 mA h g^{-1} when cycling to 6000 cycles, and the capacity retention rate is 94.3%. These results strongly prove that VN_xO_y electrode has excellent electrochemical performance. In order to further prove that the prepared VN_xO_y anode has good structural stability and electrochemical performance, the previously published zinc ion electrode materials^[1b,19] were also compared, and the results are shown in Figure 6f and Table S4, Supporting Information. It is further clarified that the

VN_xO_y electrode which transformed into amorphous phase has excellent rate performance.

In addition, the effects of crystallinity and electrolyte concentration on the electrochemical performance were also studied (Figures S13–S15, Supporting Information). We found that VN_xO_y has the best electrochemical performance when the calcination temperature is 800 °C and the concentration of electrolyte is 3 m. Further observation of the micro morphology at different temperatures (Figure S13, Supporting Information) shows that the crystallinity is very higher at 900 °C, so the required migration energy barrier is larger, which is not conducive to the insertion and desorption of zinc ions. The corresponding charge discharge curves and CV curves of 700 and 900 °C are shown in Figure S16, Supporting Information. The crystallinity of VN_xO_y with 800 °C is not very good, which is more conducive to the diffusion of zinc ions and provides higher capacity. Therefore, the material with low crystallinity is more suitable for the electrode material of water zinc ion than those with high crystallinity. Moreover, for VN_xO_y with low crystallinity, the electrochemical activation is easier to occur, so as to achieve excellent electrochemical performance.

The reaction mechanism of the VN_xO_y electrode has been elucidated by a combination study of electrochemical measurements, XRD, TEM, and XPS analyses. As we know, the overall performance of the battery, especially the rate performance, depends to a large extent on the diffusion rate of zinc

ions in the electrode material. In other words, it is necessary to study the chemical diffusion coefficient with determines the electrochemical performance of materials. The Galvanostatic Intermittent Titration Technique (GITT) was used for in-depth analysis of the Zn^{2+} diffusion coefficient (Figure S17, Supporting Information). As expected, the Zn^{2+} diffusion coefficient of VN_xO_y is an order of magnitude higher than that of $\text{VN}/\text{V}_2\text{O}_3$ and V_2O_3 electrodes (Figure 6e). In addition, the impedance of VN_xO_y in the initial state and charging to 1.6 V has also been tested (Figure S18, Supporting Information). Obviously, the R_{ct} value of the VN_xO_y electrode charged to 1.6 V (78.5 Ω) is much lower than its initial state (140.9 Ω). Moreover, the diffusion of zinc ions after electrochemical activation can be effectively promoted. According to Equation S2, Supporting Information, the diffusion coefficient of zinc ions is inversely proportional to the square of the slope σ . The slopes of the VN_xO_y electrode in the initial state and charging to 1.6 V are 83.8 and 16.8, respectively. It further proves that VN_xO_y has excellent diffusion ability after electrochemical activation.

In order to further explain the reasons for the cycle stability of VN_xO_y , the SEM, TEM, and XRD after the cycle are further analyzed. Figure 7a–c are the SEM images of VN_xO_y after 2, 50, and 300 cycles, respectively. From Figure 7c, we can see that the morphology of VN_xO_y still has a shuttle-shaped core-shell structure after 300 cycles at a current density of 200 mA g^{-1} . Figure 7d shows the XRD diffraction pattern of

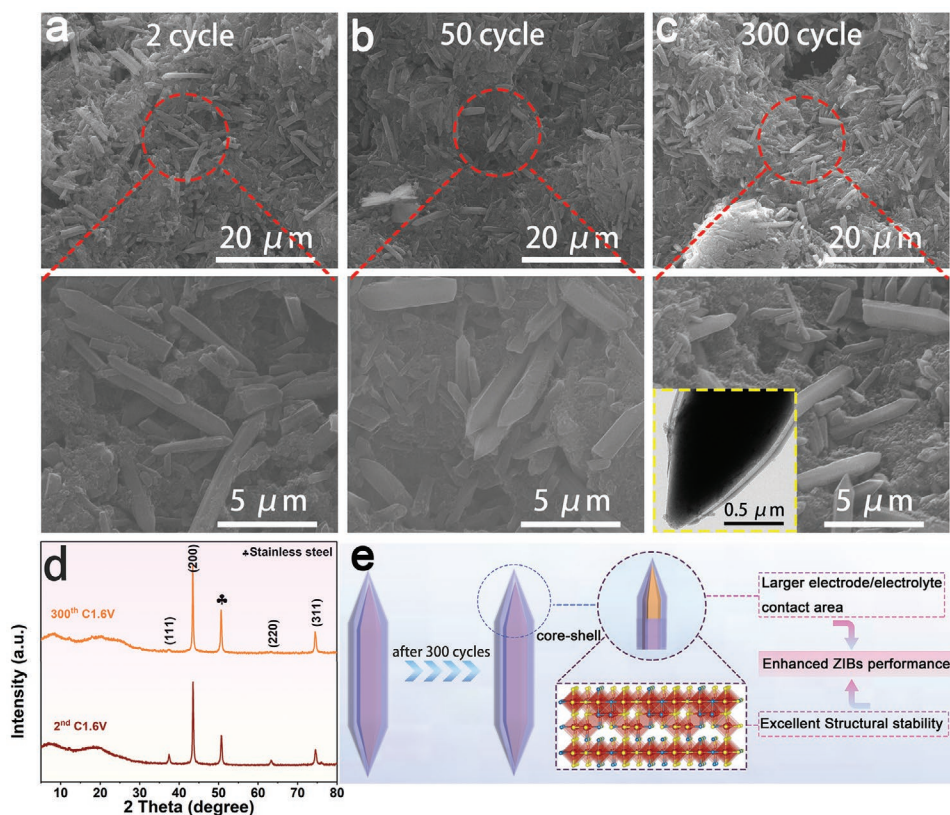


Figure 7. a–c) SEM images of VN_xO_y electrode after second, 50th, and 300th cycles, respectively. d) Ex situ XRD of VN_xO_y after different cycle. e) Schematic diagram of VN_xO_y structure.

VN_xO_y after 2 cycles and 300 cycles of charge and discharge. It can be seen that the phase has not changed significantly. It can be explained that the VN_xO_y with a shuttle-type core-shell structure has a stable structure and is suitable for the insertion and extraction of zinc ions. Figure 7e is a schematic diagram of the enlarged structure of VN_xO_y . VN_xO_y has a larger area in contact with the electrolyte, and the core-shell structure can alleviate the volume change during the insertion and extraction of the zinc ions. After several hundred cycles of charging and discharging, it still maintains the original structure. Specifically, due to the unique enhanced mass transfer structure, it can provide high specific capacity and good cycle stability for ZIBs as the cathode.

3. Conclusion

In this work, a high-performance aqueous $\text{Zn-VN}_x\text{O}_y$ battery was reported. The results show that the VN_xO_y is more suitable for storage of zinc ions after the electrochemical activation occurs during the first charging. The theoretical calculation further proves the feasibility of reversible electrochemical activation in charge discharge process. These advantages are coupled with the pseudocapacitive behavior of the cathode, which can accelerate the mass diffusion of electrons and ions, buffer the strain/stress generated during the diffusion of Zn^{2+} , and achieve high utilization of active materials. Due to the efficient energy storage mechanism, this aqueous $\text{Zn-VN}_x\text{O}_y$ battery still provides a high reversible capacity of $100.2 \text{ mA h g}^{-1}$ after 6000 cycles at 10 A g^{-1} , excellent rate capability and rapid ion diffusivity. In addition, the concentration of 3 M ZnSO_4 electrolyte is demonstrated to favor the cyclic stability. This work further clarified the principle of vanadium-based rechargeable ZIBs and pointed out the path to high-capacity water batteries, making them one of the most promising options for next-generation energy storage.

4. Experimental Section

Material Synthesis: All chemical reagents and solvents were used as received without further purification. MIL-88B(V) was synthesized by a simple hydrothermal route.^[10] In a typical procedure, 4 mmol vanadium(III) chloride (VCl_3 , 99%, Shanghai Macklin Biochemical Co., Ltd.) and 4 mmol terephthalic acid (H_2BDC , $\geq 99\%$, Sinopharm Chemical Reagent Co., Ltd.) were added to 20 mL absolute ethanol, then 4 mL hydrochloric acid ($1 \text{ mol} \cdot \text{L}^{-1}$) was added to the above solution and stirred at room temperature for half an hour. After ultrasonic treatment for 15 min, the blue suspension was further dispersed. Finally, the solution was transferred to a 100 mL Teflon lined stainless steel autoclave and heated for 2 days in an electric oven at $120 \text{ }^\circ\text{C}$. The product was centrifuged with ethanol and dried in vacuum at $50 \text{ }^\circ\text{C}$ for one night. The obtained green powder was shuttle shaped precursor of MIL-88B(V). The VN_xO_y with core-shell structure was obtained by mixing the precursor and melamine at a mass ratio of 1:4. And the powders were calcined at $800 \text{ }^\circ\text{C}$ in Ar atmosphere for 3 h. For comparison, the $\text{VN}/\text{V}_2\text{O}_3$ was prepared by adjusting the mass ratio of precursor and melamine to 1:0.5. When melamine was not added, V_2O_3 can be obtained.

Material Characterization: The XRD data of samples were determined using a Rigaku D/max 2500 X-ray powder diffractometer ($\text{Cu K}\alpha$ radiation, $\lambda = 0.15405 \text{ nm}$). The morphologies of samples were collected by SEM (FEI Nova NanoSEM 230m, 10 kV). The scan High-resolution TEM

(HRTEM) images, energy dispersive spectrometer mapping to further study the structural characterization by using TEM (Titan G2 60-300). The thermogravimetric analysis under argon atmosphere was obtained by thermal gravimetric analyzer (NETZSCH STA 449C). The data of XPS spectrum were obtained by using ESCALAB 250Xi X-ray photoelectron spectrometer (Thermo Fisher). The surface area and pore distribution of the samples were obtained by using a NOVA 4200e instrument (Quantachrome Instruments).

Electrochemical Measurement: The electrochemical properties of the samples were tested by using stainless steel button cell (CR2032). The working electrode was prepared by coating a slurry mixed with the composites, acetylene black, and polyvinylidene fluoride with the mass ratio of 7:2:1, using N-methyl-2-pyrrolidone as a dissolvent. The well-mixed slurry was coated onto stainless-steel mesh and dried in a vacuum oven at $80 \text{ }^\circ\text{C}$ for 12 h. In this paper, zinc foil was used as anode electrode. Glass fiber filter paper was applied as separator, and the electrolyte was 3 M ZnSO_4 aqueous solution.

A multi-channel battery test system (Land CT 2001A) was used to measure the electrochemical performance of coin batteries in a potential range of 0.2–1.6 V (versus Zn^{2+}/Zn). Electrochemical impedance spectroscopy was analyzed by electrochemical workstation (multi AutoLab M204, metrohm).

Computational Details: For all simulations, DFT based on the Perdew–Burke–Ernzerhof generalized gradient approximation was used as implemented in the VASP package.^[20] The ion–electron interactions were treated within the projector augmented wave method. Migration barriers for a Zn ion diffusion were calculated using the NEB method in this structure.^[21] Eight intermediate states between the first and final images of a single Zn ion diffusion event were considered. During the NEB calculation, all the structures were allowed to relax within the fixed lattice parameters. The Monkhorst–Park meshes with 0.02 \AA^{-1} k-point spacing were adopted. The energy cutoff of plane wave basis sets was set to 700 eV, and the residual force for relaxing atom positions was less than $0.01 \text{ eV}\text{\AA}^{-1}$. The convergence criterion of the total energy was 10^{-5} eV per atom. To quantitatively evaluate the ability of VN and $\text{V}_{10}\text{N}_{11}\text{O}_{21}$ to dope with Zn atom, the doping energy (ΔE) were calculated according to the below expression:

$$\Delta E_1 = E_{\text{Zn}} + E_{\text{VN}} - E_{\text{VN@Zn}} \quad (3)$$

$$\Delta E_2 = E_{\text{Zn}} + E_{\text{V}_{10}\text{N}_{11}\text{O}_{21}} - E_{\text{V}_{10}\text{N}_{11}\text{O}_{21}@Zn} \quad (4)$$

where E_{Zn} , E_{VN} , $E_{\text{VN@Zn}}$, $E_{\text{V}_{10}\text{N}_{11}\text{O}_{21}}$, and $E_{\text{V}_{10}\text{N}_{11}\text{O}_{21}@Zn}$ are the energy of the Zn atom, VN, VN of Zn doping, $\text{V}_{10}\text{N}_{11}\text{O}_{21}$, and the $\text{V}_{10}\text{N}_{11}\text{O}_{21}$ of Zn doping respectively.

The formation energy of $\text{V}_{10}\text{N}_{11}\text{O}_{21}$ was evaluated according to the below expression:

$$E_{\text{form}} = (E_{\text{VN}} + 2E_{\text{O}} - 11E_{\text{N}} - 10E_{\text{V}} - E_{\text{V}_{10}\text{N}_{11}\text{O}_{21}})/n \quad (5)$$

where E_{VN} , E_{O} , E_{N} , E_{V} , and $E_{\text{V}_{10}\text{N}_{11}\text{O}_{21}}$ are the energy of the VN, O, N, V, and $\text{V}_{10}\text{N}_{11}\text{O}_{21}$, respectively. The n is the total number of atoms.

Supporting Information

Supporting Information is available from the Wiley Online Library or from the author.

Acknowledgements

This work was supported by the Natural Science Foundation of Hunan Province in China (2018JJ1036), the National Natural Science Foundation of China (No. 51874362, 51932011, and 52072411), and Central South University Postgraduate Independent Exploration and Innovation Project (No. 1053320190537).

Conflict of Interest

The authors declare no conflict of interest.

Data Availability Statement

Research Data are not shared.

Keywords

aqueous zinc-ion batteries, electrochemical activation, long cycle life, vanadium-based cathodes, vanadium nitride

Received: April 2, 2021

Revised: June 8, 2021

Published online: September 1, 2021

- [1] a) Y. Zeng, X. Zhang, Y. Meng, M. Yu, J. Yi, Y. Wu, X. Lu, Y. Tong, *Adv. Mater.* **2017**, *29*, 1700274; b) C. Xia, J. Guo, Y. Lei, H. Liang, C. Zhao, H. N. Alshareef, *Adv. Mater.* **2018**, *30*, 1705580; c) G. Fang, J. Zhou, A. Pan, S. Liang, *ACS Energy Lett.* **2018**, *3*, 2480; d) S. Guo, L. Qin, T. Zhang, M. Zhou, J. Zhou, G. Fang, S. Liang, *Energy Storage Mater.* **2021**, *34*, 545.
- [2] a) F. Wan, Z. Niu, *Angew. Chem., Int. Ed.* **2019**, *58*, 16358; b) F. Wan, Y. Zhang, L. Zhang, D. Liu, C. Wang, L. Song, Z. Niu, J. Chen, *Angew. Chem., Int. Ed.* **2019**, *58*, 7062.
- [3] a) H. D. Yoo, Y. Liang, H. Dong, J. Lin, H. Wang, Y. Liu, L. Ma, T. Wu, Y. Li, Q. Ru, Y. Jing, Q. An, W. Zhou, J. Guo, J. Lu, S. T. Pantelides, X. Qian, Y. Yao, *Nat. Commun.* **2017**, *8*, 339; b) J. Muldoon, C. B. Bucur, T. Gregory, *Chem. Rev.* **2014**, *114*, 11683; c) T. Koketsu, J. Ma, B. J. Morgan, M. Body, C. Legein, W. Dachraoui, M. Giannini, A. Demortiere, M. Salanne, F. Dardoize, H. Groult, O. J. Borkiewicz, K. Chapman, P. Strasser, D. Dambournet, *Nat. Mater.* **2017**, *16*, 1142.
- [4] a) N. Zhang, F. Cheng, Y. Liu, Q. Zhao, K. Lei, C. Chen, X. Liu, J. Chen, *J. Am. Chem. Soc.* **2016**, *138*, 12894; b) W. Li, D. Corradini, M. Body, C. Legein, M. Salanne, J. Ma, K. W. Chapman, P. J. Chupas, A. L. Rollett, C. Julien, K. Zhagib, M. Duttine, A. Demourgues, H. Groult, D. Dambournet, *Chem. Mater.* **2015**, *27*, 5014; c) P. Gao, P. Metz, T. Hey, Y. Gong, D. Liu, D. D. Edwards, J. Y. Howe, R. Huang, S. T. Mixture, *Nat. Commun.* **2017**, *8*, 14559.
- [5] C. Xia, J. Guo, P. Li, X. Zhang, H. N. Alshareef, *Angew. Chem., Int. Ed.* **2018**, *57*, 3943.
- [6] C. Wu, S. Gu, Q. Zhang, Y. Bai, M. Li, Y. Yuan, H. Wang, X. Liu, Y. Yuan, N. Zhu, F. Wu, H. Li, L. Gu, J. Lu, *Nat. Commun.* **2019**, *10*, 73.
- [7] N. Zhang, F. Cheng, J. Liu, L. Wang, X. Long, X. Liu, F. Li, J. Chen, *Nat. Commun.* **2017**, *8*, 405.
- [8] C. Xu, B. Li, H. Du, F. Kang, *Angew. Chem., Int. Ed. Engl.* **2012**, *51*, 933.
- [9] a) J. Ding, Z. Du, B. Li, L. Wang, S. Wang, Y. Gong, S. Yang, *Adv. Mater.* **2019**, *31*, 1904369; b) C. Zhu, G. Fang, S. Liang, Z. Chen, Z. Wang, J. Ma, H. Wang, B. Tang, X. Zheng, J. Zhou, *Energy Storage Mater.* **2020**, *24*, 394; c) F. W. Fenta, B. W. Olbasa, M. C. Tsai, M. A. Weret, T. A. Zegeye, C. J. Huang, W. H. Huang, T. S. Zeleke, N. A. Sahalie, C. W. Pao, S. H. Wu, W. N. Su, H. J. Dai, B. J. Hwang, *J. Mater. Chem. A* **2020**, *8*, 17595; d) T. Koketsu, J. Ma, B. J. Morgan, M. Body, C. Legein, W. Dachraoui, M. Giannini, A. Demortiere, M. Salanne, F. Dardoize, H. Groult, O. J. Borkiewicz, K. W. Chapman, P. Strasser, D. Dambournet, *Nat. Mater.* **2017**, *16*, 1142; e) N. Zhang, Y. Dong, M. Jia, X. Bian, Y. Wang, M. Qiu, J. Xu, Y. Liu, L. Jiao, F. Cheng, *ACS Energy Lett.* **2018**, *3*, 1366; f) J. Hao, J. Mou, J. Zhang, L. Dong, W. Liu, C. Xu, F. Kang, *Electrochim. Acta* **2018**, *259*, 170.
- [10] F. Carson, J. Su, A. E. Platero-Prats, W. Wan, Y. Yun, L. Samain, X. Zou, *Cryst. Growth Des.* **2013**, *13*, 5036.
- [11] G. Fang, S. Liang, Z. Chen, P. Cui, X. Zheng, A. Pan, B. Lu, X. Lu, J. Zhou, *Adv. Funct. Mater.* **2019**, *29*, 1905267.
- [12] G. A. Sawatzky, D. Post, *Phys. Rev. B* **1979**, *20*, 1546.
- [13] H. Luo, B. Wang, F. Wang, J. Yang, F. Wu, Y. Ning, Y. Zhou, D. Wang, H. Liu, S. Dou, *ACS Nano* **2020**, *14*, 7328.
- [14] X. Yang, J. Nash, J. Anibal, M. Dunwel, S. Kattel, E. Stavitski, K. Attenkofer, J. G. Chen, Y. Yan, B. Xu, *J. Am. Chem. Soc.* **2018**, *140*, 13387.
- [15] R. Trehan, Y. Lifshitz, J. W. Rabalais, *J. Vac. Sci. Technol. A* **1990**, *8*, 4026.
- [16] G. Fang, Z. Wu, J. Zhou, C. Zhu, X. Cao, T. Lin, Y. Chen, C. Wang, A. Pan, S. Liang, *Adv. Energy Mater.* **2018**, *8*, 1703155.
- [17] a) V. Augustyn, P. Simon, B. Dunn, *Energy Environ. Sci.* **2014**, *7*, 1597; b) V. Augustyn, J. Come, M. A. Lowe, J. W. Kim, P. L. Taberna, S. H. Tolbert, H. D. Abruna, P. Simon, B. Dunn, *Nat. Mater.* **2013**, *12*, 518; c) D. Chao, P. Liang, Z. Chen, L. Bai, H. Shen, X. Liu, X. Xia, Y. Zhao, S. V. Savilov, J. Lin, Z. X. Shen, *ACS Nano* **2016**, *10*, 10211.
- [18] K. Zhang, Z. Hu, X. Liu, Z. Tao, J. Chen, *Adv. Mater.* **2015**, *27*, 3305.
- [19] a) P. He, M. Y. Yan, G. B. Zhang, R. M. Sun, L. N. Chen, Q. Y. An, L. Q. Mai, *Adv. Energy Mater.* **2017**, *7*, 1601920; b) M. H. Alfaruqi, V. Mathew, J. Song, S. Kim, S. Islam, D. T. Pham, J. Jo, S. Kim, J. P. Baboo, Z. Xiu, K. S. Lee, Y. K. Sun, J. Kim, *Chem. Mater.* **2017**, *29*, 1684; c) P. He, Y. Quan, X. Xu, M. Yan, W. Yang, Q. An, L. He, L. Mai, *Small* **2017**, *13*, 1702551; d) P. He, G. Zhang, X. Liao, M. Yan, X. Xu, Q. An, J. Liu, L. Mai, *Adv. Energy Mater.* **2018**, *8*, 1702463; e) P. Hu, T. Zhu, X. Wang, X. Wei, M. Yan, J. Li, W. Luo, W. Yang, W. Zhang, L. Zhou, Z. Zhou, L. Mai, *Nano Lett.* **2018**, *18*, 1758; f) G. Li, Z. Yang, Y. Jjiang, W. Zhang, Y. Huang, *J. Power Sources* **2016**, *308*, 52; g) W. Li, K. Wang, S. Cheng, K. Jjiang, *Energy Storage Mater.* **2018**, *15*, 14; h) T. Jiao, Q. Yang, S. Wu, Z. Wang, D. Chen, D. Shen, B. Liu, J. Cheng, H. Li, L. Ma, C. Zhi, W. Zhang, *J. Mater. Chem. A* **2019**, *7*, 16330; i) D. Feng, T.-N. Gao, L. Zhang, B. Guo, S. Song, Z. A. Qiao, S. Dai, *Nano-Micro Lett.* **2020**, *12*, 14.
- [20] a) G. Kresse, J. Furthmuller, *Phys. Rev. B: Condens. Matter Mater. Phys.* **1996**, *54*, 11169; b) J. P. Perdew, J. A. Chevary, S. H. Vosko, K. A. Jackson, M. R. Pederson, D. J. Singh, C. Fiolhais, *Phys. Rev. B: Condens. Matter Mater. Phys.* **1992**, *46*, 6671.
- [21] G. Henkelman, B. P. Uberuaga, H. Jonsson, *J. Chem. Phys.* **2000**, *113*, 9901.